The tale of two rooms: comparison of QuSpin zero-field OPMs' operation in two magnetically shielded environments

Ekaterina Skidchenko[1], Anna Butorina[1,2], Nikita Fedosov[3], Oleg Shevtsov[2,3], Daria Medvedeva[2,3], Zhao Darisy[4,5], Dubynin Ignat[4], Maxim Fedorov[1,6], Nikolay Koshev[1,2], and Alexei Ossadtchi[2,3]

[1]Skolkovo Institute Of Science And Technology
[2]LIFT, Life Improvement by Future Technologies Institute
[3]Centre for Bioelectric Interfaces Higher School of Economics
[4]Moscow State University of Psychology and Education (MEG Center)
[5]National Research Centre "Kurchatov Institute"
[6]Kharkevich Institute of Information Transmission Problems of RAS

November 19, 2024

Abstract

This paper addresses several critical aspects of using optically pumped magnetometers (OPMs), focusing on both metrological issues and the enhancement of signal quality. We present a quantitative methodology for OPM measurements standardization and quality evaluation, which is crucial in biomedical applications like magnetoencephalography (MEG). Additionally, we introduce a novel, cost-effective portable active magnetic shielding system – digital adaptive suppression system (DASS) – that represents a significant advancement over traditional analog active shielding. Through comprehensive experimental research, we evaluate first- and third-generation commercial OPMs from QuSpin Inc. in two distinct magnetic environments. Our results demonstrate that the DASS ensures optimal and reliable OPM performance, even in noisy urban settings, surpassing the effectiveness of conventional analog shielding. These findings highlight the need for advanced magnetic shielding solutions to enhance the accuracy and reproducibility of OPM measurements.

Posted on 19 Nov 2024 — CC-BY 4.0 — https://doi.org/10.36227/techrxiv.171617338.87291097/v3 — e-Prints posted on TechRxiv are preliminary reports that are not peer reviewed. They should not b...

The tale of two rooms: comparison of QuSpin zero-field OPMs' operation in two magnetically shielded environments

Ekaterina Skidchenko, Anna Butorina, Nikita Fedosov, Oleg Shevtsov, Daria Medvedeva, Darisy Zhao, Ignat Dubynin, Maxim Fedorov, Nikolay Koshev, Alexei Ossadtchi

***Abstract*—This paper addresses several critical aspects of using optically pumped magnetometers (OPMs), focusing on both metrological issues and the enhancement of signal quality. We present a quantitative methodology for OPM measurements standardization and quality evaluation, which is crucial in biomedical applications like magnetoencephalography (MEG). Additionally, we introduce a novel, cost-effective portable active magnetic shielding system – digital adaptive suppression system (DASS) – that represents a significant advancement over traditional analog active shielding. Through comprehensive experimental research, we evaluate first- and third-generation commercial OPMs from QuSpin Inc. in two distinct magnetic environments. Our results demonstrate that the DASS ensures optimal and reliable OPM performance, even in noisy urban settings, surpassing the effectiveness of conventional analog shielding. These findings highlight the need for advanced magnetic shielding solutions to enhance the accuracy and reproducibility of OPM measurements.**

***Index Terms*—Magnetoencephalography, optically pumped magnetometers, zero-field magnetic sensor, active shielding, digital adaptive suppression system, magnetic signal quality, phantom, magnetically shielded room, MEG, SQUID, OPMs, QuSpin, DASS, MSR.**

Manuscript received August 8, 2024; revised November 7, 2024. (Corresponding author: *Ekaterina Skidchenko*.)

The works on the development of the experimental methodology, experiments with QuSpin Gen-1 magnetometers, and signal processing were supported by the Russian Science Foundation under grant 22-71-10120 (https://rscf.ru/project/22-71-10120/). The works on experiments with QuSpin Gen-3 magnetometers, research on heat dissipation, and overall assistance in experiments in Moscow MEG-Center (MSUPE) were supported by the Russian Science Foundation under grant 22-19-00528 (https://rscf.ru/project/22-19-00528/). The DASS has been developed as a part of the Strategic Project "Human Brain Resilience: Neurocognitive Technologies for Adaptation, Learning, Development, and Rehabilitation in a Changing Environment," which is a component of the Higher School of Economics' development program under the "Priority 2030" academic leadership initiative.

Ekaterina Skidchenko is with Skolkovo Institute Of Science And Technology (e-mail: ekaterina.skidchenko@skoltech.ru).

Anna Butorina and Nikolay Koshev are with Skolkovo Institute Of Science And Technology and LIFT, Life Improvement by Future Technologies Institute (e-mail: a.butorina@skoltech.ru and n.koshev@skoltech.ru).

Nikita Fedosov is with Centre for Bioelectric Interfaces Higher School of Economics (e-mail:np$_f$$edosov@list.ru$).

Oleg Shevtsov, Daria Medvedeva and Alexei Ossadtchi are with LIFT, Life Improvement by Future Technologies Institute and Centre for Bioelectric Interfaces Higher School of Economics (e-mail: olegshevts@gmail.com, dariamedvedeva777@gmail.com and ossadtchi@gmail.com)

Darisy Zhao is with Moscow State University of Psychology and Education (MEG Center) and National Research Centre "Kurchatov Institute" (e-mail: chzhao@phystech.edu).

Ignat Dubynin is with Moscow State University of Psychology and Education (MEG Center) (e-mail: ignd@mail.ru).

Maxim Fedorov is with Skolkovo Institute Of Science And Technology and Kharkevich Institute of Information Transmission Problems of RAS (e-mail: fedorov@iitp.ru).

I. Introduction

OPTICALLY pumped magnetometers (OPMs) represent a significant advancement in the field of high-accuracy magnetometry, offering precise detection of weak magnetic fields across various applications. Since their commercial availability in 2017 [1], OPMs have gained recognition for enhancing the flexibility and compactness of measurement systems, particularly in challenging environments. OPMs are now utilized in areas such as geomagnetic research [2], biomedicine [3]–[10] and fundamental physics experiments [11]. OPMs are showing promise in overcoming the limitations of stationary systems based on superconducting quantum interference devices (SQUIDs), as highlighted in studies such as [12]. A key advantage of OPM technology is its capacity to be configured into flexible, close-to-surface arrays, which not only improve signal-to-noise ratios but also allow for easy adaptation to varying geometries and support the design of adaptive, task-specific spatial sampling schemes [13]. Despite their growing popularity, OPMs still require careful development of infrastructure and methodology to ensure reliable measurements. In this article, we focus on the application of OPMs in a powerful neuroimaging technique: magnetoencephalography (MEG) – a modern and effective method for the non-invasive registration of brain-induced magnetic signals.

To date, a variety of OPMs and OPM-based solutions exist. They come in different flavours with regard to the vapour cell content, e.g.: K (potassium) [14], Rb (rubidium) [1], Cs (cesium) [15] or He4 isotope [16]. OPMs can also be custom [14], [17]–[19] or commercial: QuSpin Inc. (www.quspin.com/products-qzfm/), FieldLine Inc. (www.fieldlineinc.com) and Mag4Health (www.mag4health.com). OPM-based systems can afford sparse or dense [20] head coverage.

The use of OPMs in MEG started with systems comprising low count of sensors measuring activity of the primary sensory brain areas with partial coverage [21]. Currently there already exists a palette of practically oriented multichannel OPM system demonstrations capable of epileptic activity mapping [22], registering fetal brain activity [23], measuring peripheral nervous system activity [24] and contactless measurement of retinal activity [25]. OPMs also open new possibilities to research of deep brain structures, such as hippocampus [26] and cerebellum [27], and facilitate motor system research by enabling registration of MEG in freely moving subjects [28],

[29]. Apart from empirical studies, OPMs are successfully used in simulations [13], [30], [31], and are already employed as a reference tool in developing novel sensors [32].

However, despite the great advantages of OPMs in comparison with SQUID systems the former are for now novel instrumentation and only have to go through the procedure of standardization that is becoming crucial keeping in mind future application of OPM-MEG in clinics.

From the other hand, magnetic fields generated by living organisms (not only of cerebral origin) have typically extremely low amplitudes in the femto-pico Tesla range which makes their measurement susceptible to the external electromagnetic interference and disruptive fields, such as the Earth's magnetic field (50 μT) and time-varying industrial noises. The comparison of these values underscores the challenges in biomagnetometry, highlighting the critical importance of sensor sensitivity combined with effective magnetic shielding. Practically useful operation of OPMs necessitates a controlled near-zero ambient magnetic field environments for zero-field OPMs [21], [33], [34] or creation of a directed magnetic field vector to make non-zero field OPMs measure specific magnetic field component [15], [19]. The latter helps to ensure linearity of the MEG observation equation and facilitates subsequent source localization steps.

The main aim of this research is to shed light on the main metrological issues related to OPMs and to contribute to the OPMs standardization via the implementation of the quantitative methodology of measurement quality assessment.

For this purpose we contrasted a naive use of the commercially available OPMs in the standard magnetically shielded room (MSR), providing reasonably quiet magnetic environment sufficient for a successful operation of a SQUID-based system, against deploying the OPMs in the MSR with a unique and specifically designed digital adaptive suppression system (DASS) for remnant field compensation. Many magnetic suppression systems employed not only in magnetoencephalography but in biomagnetic measurements in general are presented in the form of biplanar coils [28], [33], [35]–[37] of different shape and size, e.g. in asymmetric cylindrical implementation [38] and miniaturized [39]. Besides popular biplanar coils, there are other exciting options, such as [29], [40], [41]. Additionally it is important to mention work [42], which is the closest study to ours. However, compared to other suppression systems in addition to ensuring optimal OPM performance the advance of DASS lies in the attractive combination of valuable features: it is cheap and uses a low-end adaptive algorithm, providing at the same time volume enough to contain a whole head. Moreover, compared to analog counterparts, digital control enables easy change of system parameters and flexible signal processing capabilities.

We employed the two generations (Gen-1 and Gen-3) of the most popular commercially available OPM sensors manufactured by QuSpin Inc. and performed a set of standardized test recordings of magnetic field signals generated by a test coil and a phantom. We have systematically analyzed our observations and highlighted several sources of variability in the measured signals, most of which are caused by the lack of sufficiently stringent control over the remnant magnetic fields and the excessive reliance on the standard analog suppression system. Along with standardization methodology and unique suppression system, cross-generation analysis of QuSpin OPMs in two different magnetic environments represents additional novelty and advantage of our work. This study will hopefully help research groups who are just starting to dive into the topic of OPM-based MEG and facing excessive measurements variability issues, as well as for investors, funds, large institutions, certifying bodies (identification of areas of development and research, verification of protocols, measurement safety, etc.).

The paper is organized as follows. Section II contains a detailed description of methods that we used in our experiments including the methodology of signal quality assessment and a brief outline of the custom remnant field compensation system (DASS). The results of the experiments in two different MSRs are presented in Section III. Finally, in Section IV we provide the analysis of the results and discuss our findings. As a bonus we consider the OPMs' overheating issue and provide infrared camera based analysis of the temperature on the scalp-oriented sensor head surface for Gen-1 and Gen-3 sensors.

II. Methods

A. Sensors

In this paper we used commercial optically pumped zero-field magnetometers QZFM produced by company QuSpin Inc. (Colorado, USA) of two generations: the earliest and the latest (Gen-1 and Gen-3). Figures 1a) and 1b) show a photograph of both Gen-1 and Gen-3 sensor heads and their diagrams, respectively. Both generations have their main components (laser, rubidium vapor cell and photodetector) arranged similarly. More details on OPMs' physics can be found in the excellent reviews [14], [21].

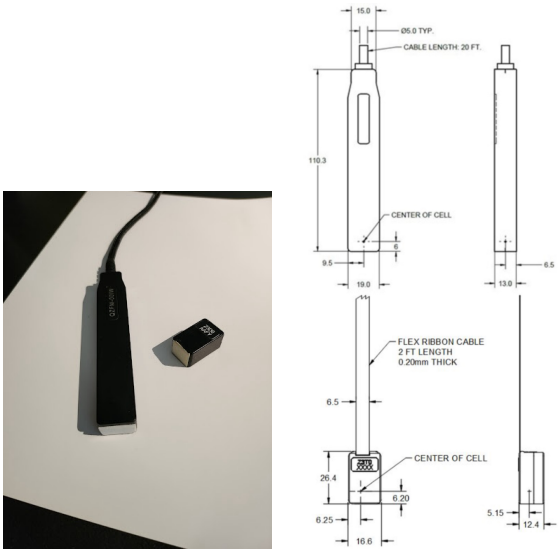

(a) (b)

Fig. 1. The QZFM OPM sensors: (a) photograph showing a comparison of Gen-1 and Gen-3 sensor heads; (b) diagrams of Gen-1 (top) and Gen-3 (bottom) (www.quspin.com/products-qzfm/).

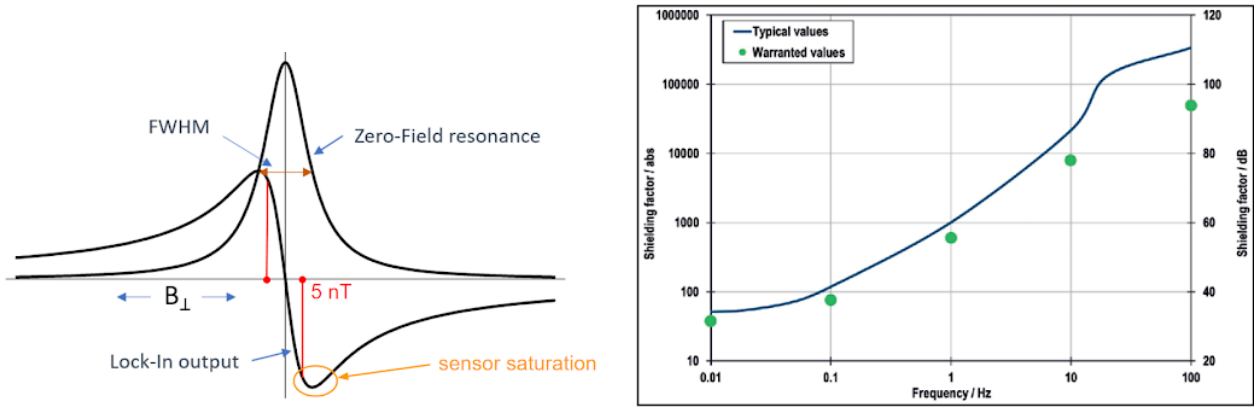

(A) (B)

Fig. 2. a) - Operational curves of the QuSpin OPM sensors. FWHM - full width at half maximum [1]; b) - Typical shielding factor of the MSR (www.vacuumschmelze.com).

Additionally, both of these sensors have two orthogonal sensitive axes. The difference between two generations is primarily in their performance and size. According to the QuSpin certificate of compliance Gen-1 magnetometers have sub $20fT/\sqrt{Hz}$ sensitivity in the frequency band of 1-100 Hz, while Gen-3 sensors (in dual axis version), according to the QuSpin website (www.quspin.com/products-qzfm/), yield field sensitivity $< 15fT/\sqrt{Hz}$ in 3-100 Hz band (typical $7-10fT/\sqrt{Hz}$). Gen-3 is not only more sensitive, but also has smaller dimensions: 12.4 x 16.6 x 26.4 mm^3 in volume in comparison with 13.0 x 19.0 x 110.3 mm^3 for Gen-1 sensors.

Optical magnetometry is paving its road to the world of biomedical applications primarily with sensors operating in the spin exchange relaxation-free (SERF) regime, see however [43] for the early pioneering developments of total field OPMs including gradientometric arrays applied for measuring weak biomagnetic fields in the 1980s. However, the use of total field magnetometers for distributed measurements aimed at localizing the corresponding sources is complicated by the non-linearity of the associated observation model. Zero-field OPMs operating in SERF regime do not have such a disadvantage and are capable of registering directional components of the magnetic field that respects the linear additivity property in the observation equation. At the same time, SERF OPMs (or zero-field OPMs) have a very narrow linear part of the operating characteristic, see Figure 2a). For the current commercially available sensors it corresponds to ± 5 nT total field which imposes harsh constraints on the environments where these sensors may remain operational and capable of reliable measurements. If the experiments are conducted in the environment where magnetic field fluctuations exceed this range the sensor measurements become uninterpretable due to sensor saturation.

B. Description of the two magnetically shielding environments

Nowadays, a layered aluminium-mu-metal magnetically shielded room (MSR) is the primary mean to suppress most of the external environmental interference signal in 0-1 kHz frequency range. The performance of these rooms is characterized by shielding factor κ, see Figure 2b), that appears to be not sufficiently high in the infra-low frequency range (see Figure 2b). For example, for a three-layer MSR the shielding factor at 100 Hz is typically around $\kappa(100) = 10^4$, while for the frequencies < 0.1 Hz the value of κ drops below $\kappa < 10^2$. Note, however, that for the strictly DC component of the field κ returns again on the order of 10^3. In practice, this leads to the leakage of the infra-slow remnant field fluctuations with peak-to-peak amplitude of about 60 nT (up to ± 20 nT) into the MSR volume. To compensate for this remnant field the dynamic suppression systems are used. Combined with the MSR they define the magnetically shielded environment where magnetic measurements are carried out. In this work we used two different magnetic suppression systems: an active shielding embedded into the walls of one MSR and an active shielding system based on the suspended Helmholtz coils implemented inside another MSR without the wall-embedded wire loops. Both rooms are manufactured by Vacuumschmelze GmbH and Co. KG (www.vacuumschmelze.com) and have similar configurations.

The first environment where we conducted our OPM experiments is the MSR containing the Elekta Neuromag SQUID system and located in the Moscow MEG center (www.megmoscow.ru/en/) (in the base floor of the Moscow State University of Psychology and Education (MSUPE)). This is rather typical that mobile OPM systems are deployed within the MSR originally built to house a legacy SQUID-based MEG system [28], [44]–[47]. The majority of such MSR rooms are built by Vacuumschmelze company (www.vacuumschmelze.com) and belong to AK-3B category of magnetic shielding solutions capable of suppressing low frequency external magnetic fields. To compensate for the drop of shielding factor in the infra-slow frequency range ($f < 0.1$ Hz), see Figure 2b), these rooms are typically equipped with active shielding coils embedded in the walls. These coils are powered by a high fidelity low noise analog amplifier and a low-pass filter used to scale and invert the signal from a reference sensor located outside the MSR at a 10-20 m distance. The scaling factor and low-pass filter cut-off frequency parameters of this analog adaptive suppression system are typically adjusted once a year during the regular

maintenance of the setup. For simplicity and convenience, we will refer to this environment as MSR room 1.

The second environment where we repeated our experiments is provided by another Vacuumschmelze AK-3B MSR recently installed in the Higher School of Economics (HSE) (www.hse.ru/en/cdm-centre/brain/). This room is used only for experiments with OPMs and other types of compact magnetometers, e.g. yttrium-iron garnet magnetometer (YIGM) [32], and does not have a SQUID-based MEG system installed inside. In contrast to the MSR room 1 the HSE's room is situated in the vibrant historic center of Moscow with a plethora of metro lines nearby and a multitude of other non-stationary urban noise sources. This MSR is not equipped with the analog suppression system and to ensure reliable operation of zero-field OPMs (e.g. QuSpin) here we implemented our digital adaptive suppression system (DASS) capable of maintaining low ambient field within the sweet-spot. We will call this environment as MSR room 2.

The diagram of our DASS is schematically drawn in Figure 3. It is based on the wire-loop coils whose current is continuously adjusted to compensate for local magnetic field fluctuations. The inner reference magnetometer (1) located at the edge of the sweet-spot zone within the Helmholtz coils measures remnant magnetic field (the error signal, the difference between the external field and the field produced by coils) together with the outer reference sensor (2), which records the outer environmental magnetic field fluctuations. These signals are then transmitted via USB to the PC, where they are transformed by the control algorithm (Figure 3) to the control signal driving the coils (3) after the digital-to-analog conversion (9). In the current implementation the control signal appears to be delayed with respect to the input signal from the inner reference sensor by 20-50 ms. The main delay sources are the data transfer and buffering delays as well as the phase response of the passive low-pass filter.

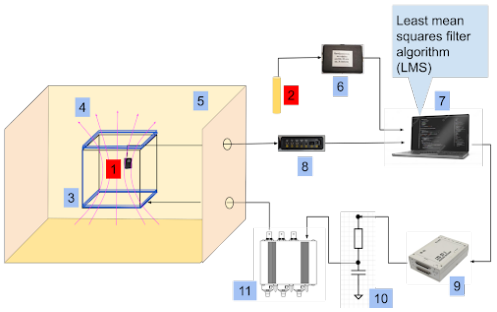

Fig. 3. Operation diagram of the digital adaptive system for suppression (DASS) of Earth's fluctuating magnetic field: 1 – the error-measurement inner reference OPM sensor; 2 – the outer reference sensor (low fidelity inductive sensor with resolution of 3 nT); 3 – carbon framework with compensation coils arranged in Helmholtz's configuration; 4 – magnetic flux generated by compensation coils (shown only for the horizontal pair of coils); 5 – magnetically shielded room; 6 – data registration block for the low fidelity inductive sensor; 7 – PC; 8 – OPM data registration block; 9 – digital-to-analog converter; 10 – control signal low-pass filter; 11 – compensation coil driver.

Fig. 4. DASS's coils installed in room 2. Each pair of Helmholtz coils comprises square coils of $1\ m \times 1\ m$ dimension located 0.5 m apart and positioned in the three orthogonal planes. The QuSpin Gen-2 OPM, that is the internal reference sensor, shown in the inset.

Each pair of Helmholtz coils comprises square coils of $1\ m \times 1\ m$ dimension located 0.5 m apart and positioned in the three orthogonal planes as shown in Figure 4. Each coil has 5 turns of copper wire, having a cross-section of 1 mm^2. The current passing through the coils generates the sweet-spot region of uniform compensating magnetic field with $0.2{\times}0.2{\times}0.2$ m^3 volume. Figure 4 shows the assembled DASS inside the MSR. Here the internal reference is the QuSpin Gen-2 OPM with two sensitive axes (see the inset in Figure 4). The internal reference sensor cancels the magnetic field component along the z-axis of the MSR.

In the core of our suppression system's control algorithm is the adaptive least mean squares (LMS) filter [48]. The external interfering field outside the MSR volume is distorted by the MSR's generally unknown transfer function (TF) so that different frequency components are suppressed with different factors. The MSR's TF can vary depending on the specific location within the room, it may also exhibit non-linear properties and vary over time which makes manually adjusted static transfer coefficients a sub-optimal solution. The dynamic LMS filter overcomes this problem, performing a real-time fit of the unknown filter coefficients using a simple update rule [48]. In essence, during its operation the LMS is continuously solving the MSR's TF identification task based on the pair of external and internal reference signals.

The algorithm for the internal reference OPM sensor and the external reference low fidelity flux-gate sensor data acquisition was implemented in Matlab and C++, respectively. The data are then sent to the LMS filtering code implemented in C++ via Lab Streaming Layer (LSL) socket protocol [49]. The digital control sequence is then converted to the analog control signal by L-Card DAC ltr35-2-8 unit with sampling rate < 100 Hz.

Typical curves characterising performance of the digital adaptive suppression system are demonstrated in Figure 5. The top panel a) shows the internal OPM measurements over two intervals: when the DASS is on and when it is off. The left bottom panel b) shows power spectral density (PSD) profiles for $f > 0$ Hz of the magnetic field outside the MSR (measured by outer reference sensor, blue), inside the MSR (measured by inner reference sensor) and DASS off (red) and inside the MSR

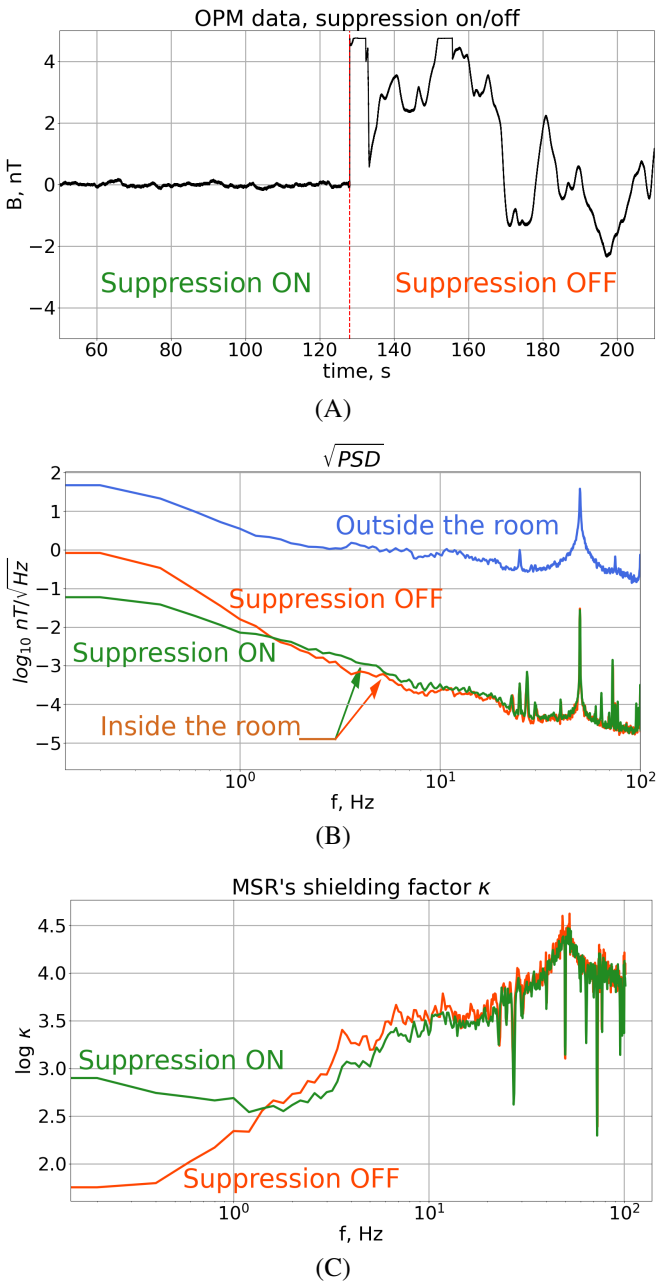

Fig. 5. Performance of the digital adaptive suppression system (DASS), room 2. The top panel a) shows the internal OPM measurements over two intervals: when the DASS is on and when it is off. The left bottom panel b) shows power spectral density (PSD) profiles for $f > 0$ Hz of the magnetic field outside the MSR (measured by outer reference sensor, blue), inside the MSR (measured by inner reference sensor) and DASS off (red) and inside the MSR and DASS on (green). The right bottom panel c) demonstrates suppression coefficient of MSR with and without DASS.

and DASS on (green). The right bottom panel c) demonstrates suppression coefficient of MSR with and without DASS.

C. Experimental setup and quality criteria

1) Phantom: In order to compare the signals obtained by two OPM generations in the magnetically shielded environment of MSR 1, we conducted a series of phantom experiments. In general, both SQUID system's dry phantom, that is often used during MEG system's maintenance, and a

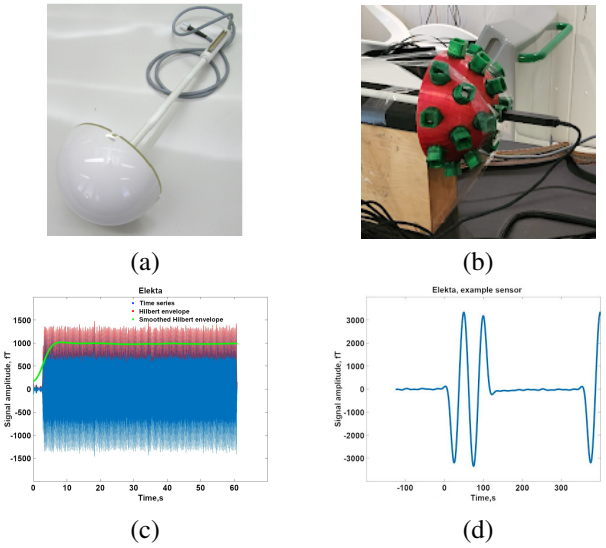

Fig. 6. Phantom experiment setup: (a) phantom [51]; (b) helmet with Gen-1 sensor placed on a phantom; (c) time series (blue line) showing phantom pattern from Elekta, the red line is the Hilbert envelope and the green line is the smoothed Hilbert envelope; (d) averaged signal from Elekta example sensor.

specially designed reference phantom can be employed for this purpose, see, for example [44] and [50], respectively.

Regardless the phantom origin, the main idea is the same: it implements calibrated current dipole sources with fixed sources' positions and orientations and produces controlled magnetic fields at specific frequencies with known magnitude.

We used a phantom supplied with Elekta Neuromag SQUID system (Neuromag, Finland) [51] (see Figure 6a), 13 and 10 pieces of Gen-1 and of Gen-3, respectively, and a universal helmet made of SBS plastic that was attached to the phantom. This phantom represents a hemisphere with 32 tangential current dipoles. During each measurement the sensors were placed one-by-one into the same helmet slot (see Figure 6b) and above the same activated current dipole (N 29) with peak-to-peak amplitude of stable 500 nAm and 20 Hz frequency (see Figure 6d). The characteristic dipole activation time series pattern is shown in Figure 6c as measured by Elekta SQUID-based system. In this case, target magnitude of the magnetic field fluctuation at the point corresponding to the sensitive element location within the sensor housing was 6.5 pT. We conducted 13-14 trials for each sensor (each lasted 1 minute).

2) Test coil: For the second series of experiments (Gen-1 sensors in MSR 2) as the standardized source of magnetic field (in MSR 2) we 3D-printed a frame for a circular test coil with 157 mm radius and 10 turns of wire, see Figure 7. The frame of the coil has a specially designed holder which allows for installing and firmly holding a QuSpin sensor for the test recordings.

In these experiments we used 5 Gen-1 sensors previously employed in room 1. During our tests we activated the test coil with a 20 Hz harmonic signal with voltage that simulates the brain magnetic activity of about 500 fT peak-to-peak. Each Gen-1 OPM sensor was placed near the center of the DASS system as shown in Figure 7. To assess the OPM sensors'

performance we recorded 1-minute long series in DASS on and off conditions, as well as around 100 trials (again each lasted 1 minute) for each of the 5 sensors with DASS on using the described setup.

3) Elekta is the gold standard: As the gold standard for our OPM results comparison we used calibrated SQUID-system Triux Elekta Neuromag (Elekta Oy, Finland) with 306 channels (102 magnetometers and 204 planar gradiometers).

When assessing sensors performance and comparing Gen-1 and Gen-3 sensors operating in the two MSRs we were primarily concerned with the following three characteristics that were our quality criteria.

- **Reliability** – reflects consistency of the experimentally measured signal produced by the phantom or the test coil with the theoretically calculated parameters. Importantly, in the case of ideal reliability of each sensor type all three types of sensors (Elekta, Gen-1 and Gen-3) should show identical results.
- **Stability** – describes the extent to which the same sensors produce similar results. For example, good stability of Gen-1 sensors means that different Gen-1 sensors during the whole experiment (one experimental day) show signal close to the theoretically expected with minimal discrepancy.
- **Reproducibility** – represents the capability of sensors results being produced in the same way across different experimental days given that all the other experimental conditions are fixed.

To aid us in visualization of these quality metrics we introduced the signal stability coefficient (SSC) measured as the standard deviation of the Hilbert envelope of the recorded test signal generated either by the phantom current dipole or the test coil. We calculated the SSCs for all three sensor groups. For Hilbert envelope please see red and green lines e.g. in Figures 6c) and 8. In 2020 the experiments were not standardized (for each experimental day the helmet was attached to the phantom anew as described in Section II-C1) and we compared only SSCs. Starting in 2022, location of the OPMs with respect to the phantom maintained fixed over all experimental days and we were able to compare signal amplitudes of two OPM generations directly. Since Elekta represents a different modality of MEG, we did not directly compare the amplitudes obtained from OPMs with amplitudes obtained from Elekta.

III. Results

As we described in Section II, first we conducted our phantom experiments in the MSR 1 (see Section II-C1). Then the OPMs were tested in the MSR 2 using the test coil setup described in Section II-C2, with the digital adaptive active suppression.

A. MSR with active shielding embedded in the MSR walls

As a starter in Figure 8 we are showing the time series of magnetic field measured by an example Gen-1 sensor in the MSR 1 in 2022. The field was generated by Elekta's phantom current dipole (index 29) activated with constant magnitude

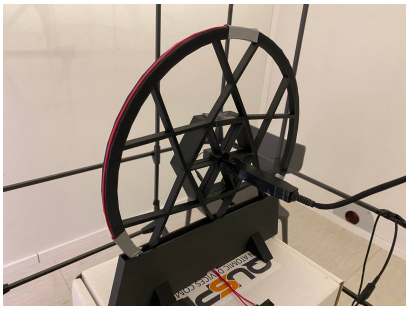

Fig. 7. Experimental setup for recording calibrated magnetic field signal from the test coil using an OPM sensor. Gen-1 QuSpin magnetometer fixed in the holder in the center of the test coil.

TABLE I
THE DISTRIBUTION OF THE SSC VALUES FOR GEN-1 AND GEN-3 SENSORS AS COMPARED TO THAT OF THE GOLD STANDARD SQUID-BASED ELEKTA SYSTEM, ROOM 1.

Metric, a.u.	Gen-1 2020	Gen-1 2022	Gen-3 2022	Elekta
average SSC	0.0584	0.2580	0.0724	0.0290
STD	0.0589	0.1413	0.0566	0.0176

II-C1 and it was supposed to have the same morphological pattern as shown in Figure 6c. However, in the midst of the recording extended for 45 seconds we can observe the undesired gradual decrease in the amplitude of the OPM measured signal outlined by the envelope (green trace). As we will conclude later, the most likely reason of such an undesired behavior of the zero-field OPM sensor is the presence of the external interference not fully accounted for by the generic adaptive remnant field compensation system the MSR 1 is equipped with.

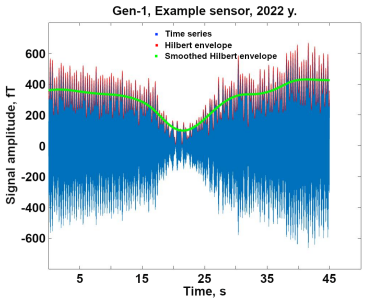

Fig. 8. The phantom pattern from the example Gen-1 sensor recorded in MEG-center MSR in 2022. The blue line is the time series, the red line is the Hilbert envelope and the green line is the smoothed Hilbert envelope.

Figure 9a) shows the SSC coefficients for Gen-1 and Gen-3 sensors as compared for the SSC of the signals registered with the gold standard Elekta SQUID system. All coefficients passed the statistical significance test. The asterisks reflect the Student's statistics, where *** - is <0.001. Since we started working with Gen-3 sensors only in year 2022 we show the results of our measurements only for this year. We can observe that all OPM measurements are characterized by significantly greater SSC values as compared to the SQUID-based MEG system recordings, see Table I for exact values.

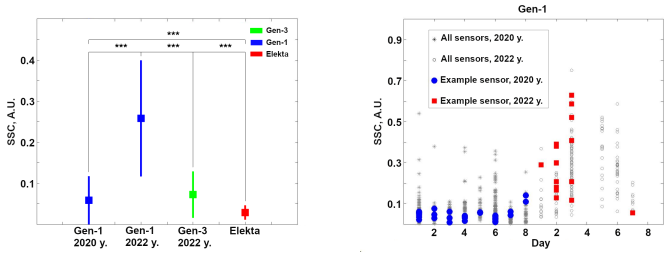

Fig. 9. (a) SSC from Gen-1 and Gen-3 sensors vs. SSC from Elekta, where the asterisks reflect the Student's statistics and *** - is <0.001; (b) comparison of SSC in 2020 and 2022 for Gen-1 sensors.

TABLE II
COMPARISON OF OPM SIGNAL AMPLITUDE FOR GEN-1 AND GEN-3 SENSORS BOTH MEASURED IN ROOM 1 IN 2022.

Metric, fT	Gen-1	Gen-3
average signal amplitude	981.7249	2.2775e+03
STD	763.7696	1.0383e+03
z-score	1.2854	2.1935

The difference between Gen-1 signal stability coefficients in 2020 and 2022 is considered more closely in the subsequent plot shown in Figure 9b. We can see that for all days of recordings Gen-1 measurements performed during year 2022 exhibit significantly higher SSC values.

Thanks to the fixed location of the OPM sensor with respect to the phantom maintained over the entire set of recordings in 2022 we could compare the magnitude of signals recorded by the two generations of sensors. In Figure 10 we compare the magnitude of OPM signals measured in 2022 by Gen-1 (blue) and Gen-2 (green) in MSR 1. Both generations are quite far from the target value (6500 fT). Although Gen-3 measurements are characterized by systematically higher amplitudes they also exhibit greater volatility, see Table II. At the same time, as evident from the corresponding z-scores reflecting the mean to standard deviation ratio, Gen-3 appears in a more favorable position as its signal magnitude is closer to the target value and exhibits smaller deviation magnitude.

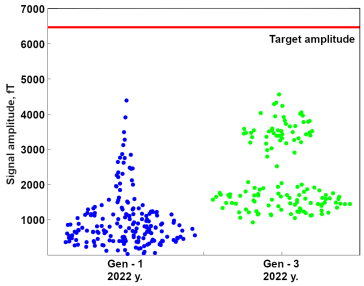

Fig. 10. OPMs signal amplitudes comparison when measuring test magnetic field signal with target magnitude of 6500 fT for Gen-1 vs. Gen-3 recorded in 2022 in MSR 1.

Finally, Figure 11 illustrates the phantom data for 2024 measured in room 1 for both Gen-1 (blue) and Gen-3 (green), where each type of figures (circle, triangle or star) represents the separate experimental day. We see the strong spread of SSC values as well as amplitude values, especially for day 2.

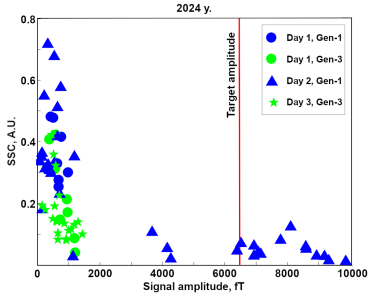

Fig. 11. Signal amplitude vs. SSC for different sensors of both generations of OPMs in different experimental days recorded in room 1 in 2024.

B. MSR with digital adaptive suppression system (DASS)

In the MSR 2, as it was described above in Section II-C2, we tested the OPM sensors with a 20 Hz test coil. Figure 12 shows the coil pattern (from the same coil but different frequency) with and without DASS, where blue reflects the signal with compensation off, while red – with compensation on. It is clearly seen that with digital adaptive suppression system we see stable signal, while in the case when compensation is off the coil constant pattern is broken.

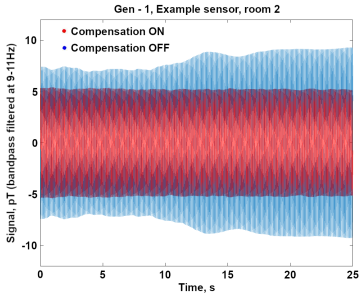

Fig. 12. The magnetic signal pattern from the 10 Hz test coil recorded by the Gen-1 example sensor with and without DASS in room 2 in 2024.

Besides checking the coil pattern, we conducted a series of experiments with five Gen-1 sensors in room 2. The results were then compared with data from Gen-1 for two years of experiments in room 1. This comparison is reflected in Figure 13a), where blue – SSC averaged for 2020 and 2022 in room 1 and red – SSC for five sensors in 2024 in room 2. Table 3 shows the corresponding values of signal stability coefficients for Gen-1 sensors tested in room 1 (MSR with active shielding embedded in MSR walls) and in room 2 (MSR with DASS). Figure 13b) shows separately the results of test coil experiments for Gen-1 sensors during two experimental days in room 2. Importantly, we use the same scale in Figure 13b) as in Figure 11.

IV. DISCUSSION

Analyzing figures in the Section III above, we can conclude that the results from all the figures lead to the same finding:

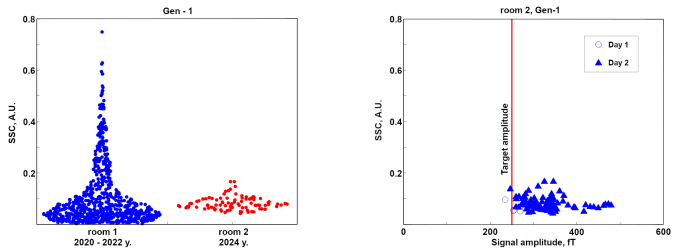

(a) (b)

Fig. 13. (a) Comparison of SSC of Gen-1 sensors in two rooms: 13 sensors averaged 2020 and 2022 in room 1 (blue) and 5 sensors in 2024 in room 2 (red). (b) Signal amplitude vs. SSC for Gen-1 OPMs measured signal from the test coil in different experimental days recorded in room 2 in 2024.

TABLE III
SIGNAL STABILITY STATISTICS FROM 13 GEN-1 SENSORS RECORDED IN ROOM 1 FOR 2020 AND 2022 (AVERAGED) AND FIVE GEN-1 SENSORS RECORDED IN ROOM 2 IN 2024.

Metric, a.u.	room 1 (MEG-center)	room 2 (HSE)
average SSC	0.1087	0.0652
STD	0.1229	0.0184

additional local active shielding, like DASS, is crucial for QuSpin OPMs regardless of their generation. Even active shielding embedded into MSR walls is not enough for optimal operation of OPMs, not to mention only MSR shielding [32]. We showed that Gen-3 sensors encounter the same issues as Gen-1 ones.

Speaking of the generations, as it can be seen on Figure 10 being tested in the same MSR (room 1) Gen-3 sensors demonstrate higher signal. Of course, the interpretation of this difference is a matter of discussion. The possible answer here is that Gen-3 is claimed to be a more robust version of QuSpin magnetometers, with improved components compared to Gen-1 (www.quspin.com/products-qzfm/). Figures 12 and 13 show the improvement of Gen-1 signal quality in room 2. We did not experiment with Gen-3 in room 2 but based on probably enhanced on-sensor coils Gen-3 will show even better signal quality improvement in room 2 than Gen-1.

Figure 9 demonstrates increased averaged SSC as well as its deviation for Gen-1 in 2022 compared to 2020. At first glance, it can be assumed that sensors deteriorate over time. However, despite the fact that the sensor deterioration factor may still be present, we believe that, first of all, it is the instability of the external magnetic field from day to day and even during one day or magnetic noise deterioration of the area in general. This is best seen in Figure 11 that shows rather controversial data for 2024, where signal stability coefficients and signal amplitudes for Gen-1 sensors drastically change within one experimental day. This is a matter of chance basically. Due to this and strong dependency of the OPMs to these field instabilities, additional local active magnetic protection is a must-have for OPMs. Thus, the results of this study can help to take a fresh look at the deterioration of the sensor signal and reveal that this deterioration may be false.

This idea is confirmed by the fact that with digital adaptive suppression system (in room 2) we observe consistency of measured values of the field amplitude with the target (theoretical) value from coil (only approx. 30% discrepancy, see Figure 13b) and all data is closely-grouped, which does not happen in room 1 while experimenting with phantom, check Figure 11. As shown in Figure 12 DASS allows OPMs to work optimally and save the stable signal pattern on the whole time range compared to the broken pattern obtained in room 1 and depicted in Figure 8. Importantly, the data obtained in the MSR room 2 meets all three signal quality characteristics (reliability, stability and reproducibility) mentioned in Section II-C3.

To summarize, ensuring the proper magnetic suppression is a top priority for OPM research initialization. This is so important that from a rational point of view it probably does not even make sense to spend money on MSR if there is no local active suppression included/planned, regardless of MSR size (standard or light). We used the example of QuSpin OPM magnetometers, but undoubtedly this rule applies to any SERF sensor. There is a reason to use SQUID system-free MSR. Installed local active shielding systems will interfere with access to the SQUID system. On the other hand, constant assembly and disassembly of the suppression system will increase the time of experimental preparation and accelerate the wear of equipment. Both aspects are inconvenient and undesirable.

Overheating

As a bonus, our additional goal was to cover the overheating problem with OPMs that appeared with Gen-1 [52] and to find out whether it was solved for Gen-3.

The temperature of the sensor's housing was measured in the MSR 1 by an infrared camera near the vapor cell (which is meant to be in close proximity to the scalp). It was done for nine pairs of Gen-1 + Gen-3 (pairs were stuck together by tape). The average temperature of Gen-1 housing near the cell was 55.6°C against 71.9°C in the case of Gen-3 (see Figure 14).

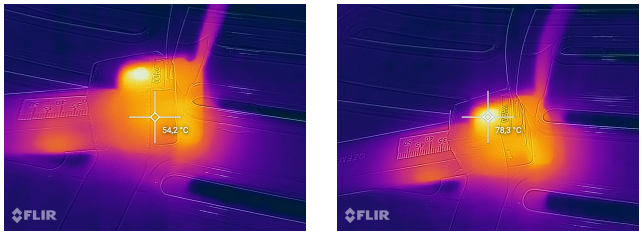

(a) (b)

Fig. 14. Temperature of sensor heads (scalp-oriented sensor surface) in one example pair: (a) Gen-1, (b) Gen-3.

We can conclude that overheating worsened in Gen-3. As it was noted in [6], such levels of temperature are above the temperature of protein coagulation which undoubtedly will not contribute to the comfort of the subjects. The vapor cell in QuSpin OPMs is heated to approx. 150°C, which is actually needed to maintain optimal performance of any Rb OPMs [34]. However, the intense warming of the housing is probably due to less successful design. The power consumption is the

same for both generations: 0.7 W/sensor head. Nonetheless, Gen-1 has a larger surface, which provides better heat dissipation. It is important to note that not all OPMs have the overheating problem. For example, even though helium OPMs can offer less sensitivity than alkali metals-based OPMs (only about $40fT/\sqrt{Hz}$ vs. $< 10fT/\sqrt{Hz}$), they operate at room temperature [53]. Nevertheless, QuSpin OPMs are a useful tool in MEG and this issue undoubtedly has to be solved.

Apparently, the scalp temperature can be kept comfortable by a judicious helmet design and proper insulation [54]. However, the situation will worsen with the transition towards dense systems. 3-axial sensors cannot solve this issue since, e.g., 50 sensors (150 channels) emit a big amount of heat (about 35 W). Probably, improvements in the sensor design can help overcome this problem. Moreover, insulation of any kind (foamed or felt) negates the advantage of OPMs over SQUIDs – their closeness to the scalp. As it was proposed in [54] in future MEG systems based on OPMs may require cold air or water for active cooling of the helmet.

Nevertheless, it is gratifying that researchers started to openly share issues connected to overheating as well as other challenges they encounter while working with OPMs, study them and try to find possible solutions, e.g. [55].

V. Conclusion

In this study, using the example of QuSpin magnetometers of two generations and experiments with phantom and test coil we experimentally showed that proper magnetic suppression is crucial for SERF, i.e. zero-field, OPMs. We demonstrated that MSR with the installed digital adaptive suppression system, as opposed to the MSR containing SQUID system and active shielding embedded into the MSR walls, provides the optimal level for OPMs operation.

Hopefully, our advice will be advantageous and help newcomers to build their own MEG systems based on OPMs and, in particular, reveal false sensor deterioration if found. Speaking more widely, without proper magnetic suppression there will be no success biomagnetometry. No matter which parts of the body/organisms we want to study: brain, eyes, heart, muscles, spinal cord; humans, fetus, rats, etc.

In our future work we will aim to test Gen-3 sensors in the MSR 2 and clarify the legitimacy of joint measurements by different generations of QuSpin sensors, and will improve our digital adaptive suppression system. It will allow to conduct more sophisticated neurophysiological experiments in order to expand the range of OPM applications.

References

[1] J. Osborne, J. Orton, O. Alem, V. Shah, Fully integrated standalone zero field optically pumped magnetometer for biomagnetism, in: Steep Dispersion Engineering and Opto-Atomic Precision Metrology XI, Vol. 10548, International Society for Optics and Photonics, 2018, p. 105481G.

[2] Y. Lu, T. Zhao, W. Zhu, L. Liu, X. Zhuang, G. Fang, X. Zhang, Recent progress of atomic magnetometers for geomagnetic applications, Sensors 23 (11) (2023). doi:10.3390/s23115318.
URL https://www.mdpi.com/1424-8220/23/11/5318

[3] H. Eswaran, D. Escalona-Vargas, E. H. Bolin, J. D. Wilson, C. L. Lowery, Fetal magnetocardiography using optically pumped magnetometers: a more adaptable and less expensive alternative?, Prenatal diagnosis 37 (2) (2017) 193–196.

[4] S. Strand, W. Lutter, J. F. Strasburger, V. Shah, O. Baffa, R. T. Wakai, Low-cost fetal magnetocardiography: a comparison of superconducting quantum interference device and optically pumped magnetometers, Journal of the American Heart Association 8 (16) (2019) e013436.

[5] M. A. Schellpfeffer, J. F. Strasburger, O. Baffa, S. A. Strand, W. Lutter, T. Phan, R. T. Wakai, Dynamics of the use of magnetocardiography in the study of the cardiac conduction system of the chick embryo, Birth Defects Research 112 (20) (2020) 1825–1833.

[6] E. Elzenheimer, H. Laufs, W. Schulte-Mattler, G. Schmidt, Magnetic measurement of electrically evoked muscle responses with optically pumped magnetometers, IEEE Transactions on Neural Systems and Rehabilitation Engineering 28 (3) (2020) 756–765.

[7] O. Baffa, R. Matsuda, S. Arsalani, A. Prospero, J. Miranda, R. Wakai, Development of an optical pumped gradiometric system to detect magnetic relaxation of magnetic nanoparticles, Journal of Magnetism and Magnetic Materials 475 (2019) 533–538.

[8] A. Prospero, J. Miranda, O. Baffa, Opm gradiometer for magnetorelaxometry, Flexible High Performance Magnetic Field Sensors: On-Scalp Magnetoencephalography and Other Applications (2022) 227–245.

[9] A. Jaufenthaler, T. Sander, P. Schier, K. Pansegrau, F. Wiekhorst, D. Baumgarten, Human head sized magnetorelaxometry imaging of magnetic nanoparticles with optically pumped magnetometers—a feasibility study, Journal of Magnetism and Magnetic Materials (2024) 171983.

[10] A. Jaufenthaler, T. Kornack, V. Lebedev, M. E. Limes, R. Körber, M. Liebl, D. Baumgarten, Pulsed optically pumped magnetometers: Addressing dead time and bandwidth for the unshielded magnetorelaxometry of magnetic nanoparticles, Sensors 21 (4) (2021) 1212.

[11] Y. J. Kim, I. Savukov, Applications of optically pumped magnetometers in fundamental physics and biophysics, in: APS March Meeting Abstracts, Vol. 2023, 2023, pp. T00–279.

[12] R. M. Hill, E. Boto, M. Rea, N. Holmes, J. Leggett, L. A. Coles, M. Papastavrou, S. K. Everton, B. A. Hunt, D. Sims, et al., Multi-channel whole-head opm-meg: Helmet design and a comparison with a conventional system, NeuroImage 219 (2020) 116995.

[13] L. Beltrachini, N. von Ellenrieder, R. Eichardt, J. Haueisen, Optimal design of on-scalp electromagnetic sensor arrays for brain source localisation, Human brain mapping 42 (15) (2021) 4869–4879.

[14] P. D. Schwindt, C. N. Johnson, Atomic magnetometer for human magnetoencephalography, Sandia Report SAND2010-8443 (2010).

[15] M. V. Petrenko, S. P. Dmitriev, A. S. Pazgalev, A. E. Ossadtchi, A. K. Vershovskii, Towards the non-zero field cesium magnetic sensor array for magnetoencephalography, IEEE Sensors Journal 21 (17) (2021) 18626–18632.

[16] W. Fourcault, R. Romain, G. Le Gal, F. Bertrand, V. Josselin, M. Le Prado, E. Labyt, A. Palacios-Laloy, Helium-4 magnetometers for room-temperature biomedical imaging: toward collective operation and photon-noise limited sensitivity, Optics Express 29 (10) (2021) 14467–14475.

[17] A. Borna, T. R. Carter, J. D. Goldberg, A. P. Colombo, Y.-Y. Jau, C. Berry, J. McKay, J. Stephen, M. Weisend, P. D. Schwindt, A 20-channel magnetoencephalography system based on optically pumped magnetometers, Physics in Medicine & Biology 62 (23) (2017) 8909.

[18] A. Borna, T. R. Carter, A. P. Colombo, Y.-Y. Jau, J. McKay, M. Weisend, S. Taulu, J. M. Stephen, P. D. Schwindt, Non-invasive functional-brain-imaging with an opm-based magnetoencephalography system, Plos one 15 (1) (2020) e0227684.

[19] M. Limes, E. Foley, T. Kornack, S. Caliga, S. McBride, A. Braun, W. Lee, V. Lucivero, M. Romalis, Portable magnetometry for detection of biomagnetism in ambient environments, Physical Review Applied 14 (1) (2020) 011002.

[20] E. J. Pratt, M. Ledbetter, R. Jiménez-Martínez, B. Shapiro, A. Solon, G. Z. Iwata, S. Garber, J. Gormley, D. Decker, D. Delgadillo, et al., Kernel flux: a whole-head 432-magnetometer optically-pumped magnetoencephalography (op-meg) system for brain activity imaging during natural human experiences, in: Optical and Quantum Sensing and Precision Metrology, Vol. 11700, SPIE, 2021, pp. 162–179.

[21] T. M. Tierney, N. Holmes, S. Mellor, J. D. López, G. Roberts, R. M. Hill, E. Boto, J. Leggett, V. Shah, M. J. Brookes, et al., Optically pumped magnetometers: From quantum origins to multi-channel magnetoencephalography, NeuroImage 199 (2019) 598–608.

[22] M. Pedersen, D. F. Abbott, G. D. Jackson, Wearable opm-meg: A changing landscape for epilepsy, Epilepsia 63 (11) (2022) 2745–2753.

[23] J. Frohlich, T. Bayne, J. S. Crone, A. DallaVecchia, A. Kirkeby-Hinrup, P. A. Mediano, J. Moser, K. Talar, A. Gharabaghi, H. Preissl, Not with a "zap" but with a "beep": measuring the origins of perinatal experience: Origins of perinatal experience, NeuroImage (2023) 120057.

[24] Y. Bu, J. Prince, H. Mojtahed, D. Kimball, V. Shah, T. Coleman, M. Sarkar, R. Rao, M. Huang, P. Schwindt, et al., Peripheral nerve magnetoneurography with optically pumped magnetometers, Frontiers in Physiology 13 (2022) 798376.

[25] B. U. Westner, J. I. Lubell, M. Jensen, S. Hokland, S. S. Dalal, Contactless measurements of retinal activity using optically pumped magnetometers, NeuroImage 243 (2021) 118528.

[26] T. M. Tierney, A. Levy, D. N. Barry, S. S. Meyer, Y. Shigihara, M. Everatt, S. Mellor, J. D. Lopez, S. Bestmann, N. Holmes, et al., Mouth magnetoencephalography: A unique perspective on the human hippocampus, NeuroImage 225 (2021) 117443.

[27] C.-H. Lin, T. M. Tierney, N. Holmes, E. Boto, J. Leggett, S. Bestmann, R. Bowtell, M. J. Brookes, G. R. Barnes, R. C. Miall, Using optically pumped magnetometers to measure magnetoencephalographic signals in the human cerebellum, The Journal of physiology 597 (16) (2019) 4309–4324.

[28] E. Boto, N. Holmes, J. Leggett, G. Roberts, V. Shah, S. S. Meyer, L. D. Muñoz, K. J. Mullinger, T. M. Tierney, S. Bestmann, et al., Moving magnetoencephalography towards real-world applications with a wearable system, Nature 555 (7698) (2018) 657–661.

[29] S. Mellor, T. M. Tierney, R. A. Seymour, R. C. Timms, G. C. O'Neill, N. Alexander, M. E. Spedden, H. Payne, G. R. Barnes, Real-time, model-based magnetic field correction for moving, wearable meg, NeuroImage 278 (2023) 120252.

[30] E. Skidchenko, A. Butorina, M. Ostras, P. Vetoshko, A. Kuzmichev, N. Yavich, M. Malovichko, N. Koshev, Yttrium-iron garnet magnetometer in meg: Advance towards multi-channel arrays, Sensors 23 (9) (2023) 4256.

[31] A. Razorenova, E. Skidchenko, A. Butorina, N. Koshev, On-scalp yttrium-iron garnet sensor arrays for brain source localization: Cramér-rao bound analysis, in: Journal of Physics: Conference Series, Vol. 2701, IOP Publishing, 2024, p. 012061.

[32] N. Koshev, A. Butorina, E. Skidchenko, A. Kuzmichev, A. Ossadtchi, M. Ostras, M. Fedorov, P. Vetoshko, Evolution of meg: A first meg-feasible fluxgate magnetometer, Human Brain Mapping 42 (15) (2021) 4844–4856. arXiv:https://onlinelibrary.wiley.com/doi/pdf/10.1002/hbm.25582, doi:https://doi.org/10.1002/hbm.25582.
URL https://onlinelibrary.wiley.com/doi/abs/10.1002/hbm.25582

[33] Z. Ding, Z. Huang, M. Pang, B. Han, Design of bi-planar coil for acquiring near-zero magnetic environment, IEEE Transactions on Instrumentation and Measurement 71 (2022) 1–10.

[34] S. Zhang, J. Lu, M. Ye, Y. Zhou, K. Yin, F. Lu, Y. Yan, Y. Zhai, Optimal operating temperature of miniaturized optically pumped magnetometers, IEEE Transactions on Instrumentation and Measurement 71 (2022) 1–7.

[35] N. Holmes, J. Leggett, E. Boto, G. Roberts, R. M. Hill, T. M. Tierney, V. Shah, G. R. Barnes, M. J. Brookes, R. Bowtell, A bi-planar coil system for nulling background magnetic fields in scalp mounted magnetoencephalography, NeuroImage 181 (2018) 760–774.

[36] N. Holmes, T. M. Tierney, J. Leggett, E. Boto, S. Mellor, G. Roberts, R. M. Hill, V. Shah, G. R. Barnes, M. J. Brookes, et al., Balanced, bi-planar magnetic field and field gradient coils for field compensation in wearable magnetoencephalography, Scientific reports 9 (1) (2019) 14196.

[37] J. Yang, X. Zhang, B. Han, J. Wang, L. Wang, Design of biplanar coils for degrading residual field in magnetic shielding room, IEEE Transactions on Instrumentation and Measurement 70 (2021) 1–10.

[38] B. Han, W. Zhou, X. Xu, J. Sun, F. Zhao, Q. Jiang, J. Qin, Asymmetric cylindrical coils design for uniform magnetic field, IEEE Transactions on Instrumentation and Measurement (2023).

[39] S. Tang, J. Lu, B. Sun, S. Wang, K. Wang, X. Zhang, B. Li, Optimal design of self-shielded biplanar coil assembly with miniaturized structure, IEEE Transactions on Instrumentation and Measurement (2023).

[40] A. Jodko-Władzińska, K. Wildner, T. Pałko, M. Władziński, Compensation system for biomagnetic measurements with optically pumped magnetometers inside a magnetically shielded room, Sensors 20 (16) (2020) 4563.

[41] T. Long, X. Song, Z. Duan, Y. Suo, Z. Wu, L. Jia, B. Han, Suppression of amplitude and phase errors in optically pumped magnetometers using dual-pi closed-loop control, IEEE Transactions on Instrumentation and Measurement (2023).

[42] Y. Wei, L. Cheng, Y. Niu, S. Chen, C. Ye, Nested magnetic field compensation with regulated coefficients for bio-magnetic field measurement, IEEE Transactions on Instrumentation and Measurement 72 (2023) 1–9.

[43] I. Kholodov, A. N. Kozlov, A. M. Gorbach, Magnetic fields of biological objects.

[44] R. Zetter, J. Iivanainen, L. Parkkonen, Optical co-registration of mri and on-scalp meg, Scientific Reports 9 (1) (2019) 5490.

[45] T. P. Gutteling, M. Bonnefond, T. Clausner, S. Daligault, R. Romain, S. Mitryukovskiy, W. Fourcault, V. Josselin, M. Le Prado, A. Palacios-Laloy, et al., A new generation of opm for high dynamic and large bandwidth meg: the 4he opms—first applications in healthy volunteers, Sensors 23 (5) (2023) 2801.

[46] J.-M. Badier, D. Schwartz, C.-G. Bénar, K. Kanzari, S. Daligault, R. Romain, S. Mitryukovskiy, W. Fourcault, V. Josselin, M. Le Prado, et al., Helium optically pumped magnetometers can detect epileptic abnormalities as well as squids as shown by intracerebral recordings, Eneuro 10 (12) (2023).

[47] J. Zerfowski, Optically pumped magnetometers for a brain-computer interface based on event-related desynchronization, Master's thesis, Donders Insitute for Brain, Cognition and Behaviour (2022).

[48] S. S. Haykin, Adaptive filter theory, Pearson Education India, 2002.

[49] LSL socket protocol, https://github.com/sccn/labstreaminglayer, [Accessed 20-June-2024].

[50] F. Cao, N. An, W. Xu, W. Wang, W. Li, C. Wang, M. Xiang, Y. Gao, X. Ning, Optical co-registration method of triaxial opm-meg and mri, IEEE Transactions on Medical Imaging (2023).

[51] E. N. Oy, Elekta Neuromag System Hardware User's Manual, Revision G, 2005.

[52] E. Skidchenko, A. Butorina, N. Koshev, How to build op-meg: Specific issues and challenges, International Journal of Psychophysiology 168 (2021) S121.

[53] S. Zahran, M. Mahmoudzadeh, F. Wallois, N. Betrouni, P. Derambure, M. Le Prado, A. Palacios-Laloy, E. Labyt, Performance analysis of optically pumped 4he magnetometers vs. conventional squids: From adult to infant head models, Sensors 22 (8) (2022) 3093.

[54] M. J. Brookes, J. Leggett, M. Rea, R. M. Hill, N. Holmes, E. Boto, R. Bowtell, Magnetoencephalography with optically pumped magnetometers (opm-meg): the next generation of functional neuroimaging, Trends in Neurosciences 45 (8) (2022) 621–634.

[55] M. Pang, Z. Huang, H. Wu, Z. Ding, B. Han, Thermal analysis of wearable opm-meg array system for auditory evoked experiments, IEEE Sensors Journal 22 (5) (2022) 4514–4523.